Chemical Science

ROYAL SOCIETY OF CHEMISTRY

EDGE ARTICLE

View Article Online
View Journal | View Issue

Cite this: *Chem. Sci.*, 2022, **13**, 6704

All publication charges for this article have been paid for by the Royal Society of Chemistry

A MXene-derived redox homeostasis regulator perturbs the Nrf2 antioxidant program for reinforced sonodynamic therapy†

Huan Wang, ‡[a] Xinchen Liu,‡[b] Xiangyu Yan,[c] Jiawen Fan,[a] Daowei Li,[d] Jinsong Ren *[a] and Xiaogang Qu *[a]

Received 20th December 2021
Accepted 25th April 2022

DOI: 10.1039/d1sc07073h

rsc.li/chemical-science

Ultrasound (US)-mediated sonodynamic therapy (SDT) has emerged as a spatiotemporally controllable therapeutic modality in combating cancer because of its high tissue-penetration depth and minimal invasiveness. However, the elevated nuclear factor erythroid 2-related factor 2 (Nrf2) antioxidant program in cancer cells can serve as a chief reactive oxygen species (ROS) detoxification system to alleviate oxidative injury and promote tumorigenesis, and thus greatly antagonize the therapeutic efficacy of ROS-mediated anticancer therapies. Herein, we report that vanadium carbide MXene-derived carbon dots (PMQDs) can act as high-efficacy sonosensitizers to efficiently generate ROS upon US irradiation and simultaneously hinder the Nrf2 antioxidant program for enhanced sonodynamic therapy of cancer. These PMQDs show superior US-triggered ROS generating ability because of their efficient migration/separation of electron–hole pairs and narrow bandgap. Importantly, these PMQDs can serve as efficient redox homeostasis regulators to perturb the Nrf2 antioxidant mechanism and thus reduce its effects on ROS neutralization for enhanced SDT efficacy. Overall, the present study will not only provide a new paradigm to augment SDT by perturbing the Nrf2 antioxidant program, but also give valuable insights into developing high-efficacy MXene-derived nanoagents for cancer therapy.

Introduction

Sonodynamic therapy (SDT) has attracted increasing interest in cancer therapy due to its distinctive properties including minimal invasiveness, high tumor specificity, and high therapeutic efficacy, and employs sonosensitizers to generate cytotoxic ROS at the focal point under ultrasound (US) irradiation.[1–3] Unlike photodynamic therapy (PDT) based on optics, US shows much deeper tissue-penetration depth, enabling SDT to ablate tumors embedded in deep tissues and organs.[4] Thus far, various kinds of sonosensitizers, including organic molecules and inorganic nanoagents, have been investigated for SDT.[4–10] However, therapeutic efficacies are still far from satisfactory.

One of the major challenges faced by sonosensitizers is that cancer cells have developed an enhanced antioxidant defense system to maintain the reductive environment needed to navigate the stresses of rapid proliferation and the hostile microenvironment.[11] Such a protective system confers oxidative stress resistance in cancer cells to combat therapeutics that rely on inducing oxidative stress. The transcription factor, nuclear factor erythroid 2-related factor 2 (Nrf2), is regarded as a master regulator of genes encoding numerous antioxidant enzymes, such as NAD(P)H quinone dehydrogenase 1 (NQO1) and heme oxygenase-1 (HO-1), *via* binding antioxidant-response elements (AREs) in response to oxidative stress.[12,13] The elevated Nrf2/ARE antioxidant mechanism in cancer cells neutralizes intracellular ROS and confers a more reduced intracellular environment, and thus antagonizes the therapeutic efficacy of ROS-mediated anticancer therapies.[14–16] Additionally, a high Nrf2 level in cancer cells is associated with poor prognosis.[17,18] Thus, the Nrf2 antioxidant system can represent a promising target to improve the SDT efficacy.

Carbon dots (CDs) hold great promise in biomedical applications owing to their high stability, abundant low-cost sources, good biosafety, and unique physicochemical properties.[19–27] In particular, the band structure of CDs with the quantum confinement effect can be finely regulated by structure engineering including size and composition engineering, suggesting their potential in SDT.[28–30] So far, a variety of small

[a]*State Key Laboratory of Rare Earth Resources Utilization and Laboratory of Chemical Biology, Changchun Institute of Applied Chemistry, Chinese Academy of Sciences, Changchun 130022, P. R. China. E-mail: jren@ciac.ac.cn; xqu@ciac.ac.cn*

[b]*Department of Endodontics, Hospital of Stomatology, Jilin University, Changchun 130021, P. R. China*

[c]*State Key Laboratory of Powder Metallurgy, Central South University, Changsha 410083, P. R. China*

[d]*Jilin Provincial Key Laboratory of Tooth Development and Bone Remodeling, Hospital of Stomatology, Jilin University, Changchun 130021, P. R. China*

† Electronic supplementary information (ESI) available. See https://doi.org/10.1039/d1sc07073h

‡ These authors contributed equally to this work.

molecules and polymers, as well as biomass, have been used as carbon precursors for CD preparation, rapidly leading to a large family of CDs with versatile architectures. Notably, the properties of CDs are closely related to the type of precursor used in the synthetic process. Recently, an emerging class of layer-structured materials including transition metal carbides and nitrides (MXenes) have been developed by selectively etching MAX-phase ceramics with the general chemical formula $M_{n+1}AX_n$ (n = 1–3), where M represents an early transition metal, X represents carbon, nitrogen, or their blend, and A represents an element from the IIIA–IVA groups.[31,32] Notably, MXenes with exposed terminal metal sites can result in versatile properties, providing desired effects for biological uses.[33,34] Recent studies have demonstrated that vanadium(v) exposure significantly reduces the gene expression of Nrf2, thus reducing the cellular antioxidant capacity by reducing the expression of downstream antioxidant enzymes.[35,36] Inspired by the above attractive features, herein we report the preparation of high-efficacy sonodynamic CDs (PMQDs) by using vanadium carbide MXene as the carbon source. Due to the efficient migration/separation of electron–hole pairs and the narrow bandgap, these PMQDs exhibited superior US-triggered ROS generating ability compared with that of the classical sonosensitizer, nano-TiO_2. Significantly, the vanadium oxide species on PMQDs could perturb the Nrf2/ARE antioxidant mechanism and thus reduce its effects on ROS neutralization to strengthen the SDT efficacy *via* reducing the expression of Nrf2 and downstream antioxidant enzymes such as NQO1 and HO-1, favoring ROS-mediated cancer therapy (Fig. 1a). Additionally, the vanadium(v) on PMQDs endowed them with glutathione (GSH) depletion properties. All these collective properties of PMQDs highlight their promise as potent nanoagents for both cellular

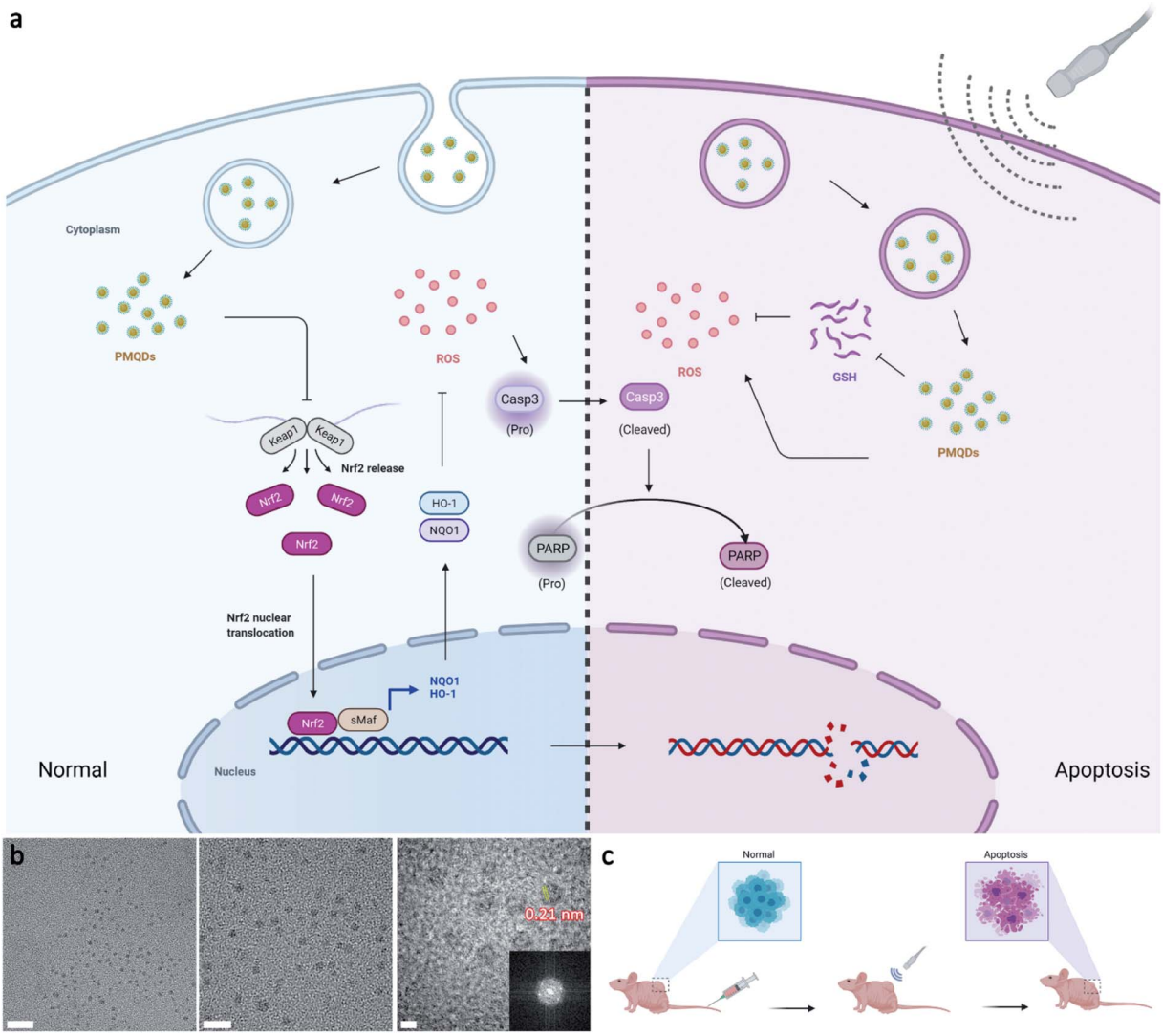

Fig. 1 Characterization and properties of MXene-derived CDs. Schematic illustration of the application of PMQDs as high-efficacy sonosensitizers to efficiently generate ROS upon US irradiation and hinder the tumor antioxidant program in cancer cells (a). Created with BioRender.com. TEM and HR-TEM images of VCQDs (b). Scale bars are equal to 20 nm, 10 nm, and 2 nm from left to right. Inset: the fast Fourier transform pattern of VCQDs. Schematic illustration of the application of PMQDs for enhanced SDT of cancer in tumor-bearing mice (c). Created with BioRender.com.

antioxidant program hindrance and effective ROS generation to enhance SDT efficacy.

Results and discussion

Layer-structured V_2C MXene was first prepared by selectively etching the Al in the V_2AlC MAX phase with hydrofluoric acid, which was characterized by powder X-ray diffraction (PXRD) and scanning electron microscopy (SEM) as shown in Fig. 2a and S2.†[37] Afterwards, CDs made from V_2C MXene (denoted as VCQDs) were synthesized *via* an ultrasonic/hydrothermal hybrid process (Fig. S1†). Transmission electron microscope (TEM) images indicated that these VCQDs were homogeneous with an average size of 2.51 nm (Fig. 1b and S3†). The high-resolution TEM (HR-TEM) image indicated that these VCQDs had fine crystallinity with a lattice spacing of 0.21 nm, which could be attributed to the characteristic diffraction planes of the sp^2 graphitic carbon. The fast Fourier transform (FFT) pattern showed that VCQDs possessed a hexagonal crystalline structure, which was in agreement with the six-fold symmetry feature of graphene.[38] Moreover, the PXRD pattern of the VCQDs showed broadened characteristic diffractions of graphitic carbon (Fig. 2b).[39] High-resolution XPS spectra were used to explore the chemical states of C, O, and V elements in V_2C MXene and VCQDs in detail. Compared with V_2C MXene, the C–V peak disappears completely in the C 1s region of VCQDs (Fig. 2c and d).[40,41] Additionally, a dramatic increase in the intensities of the C–O and COOH signals could be observed.[38] The vanished C–V bonds and the increased contents of C–O/COOH species could be attributed to the oxidation of V_2C MXene. Indeed, significantly increased contents of C–O/COOH species could also be identified in the O 1s region of VCQDs (Fig. 2g and h). The oxidation of V_2C MXene as well as the valence change of V were further investigated by V 2p XPS (Fig. 2e and f). The content of $V^{\delta+}$ species from V–C bonds was high in V_2C MXene. For VCQDs, a negligible amount of $V^{\delta+}$ species could be identified in the V 2p region, and the high valence V species including V^{4+} and V^{5+} were dominant, which could be attributed to the mixed vanadium oxide (VO_x) species.[40–43] Moreover, a negligible amount of F could be detected in the F 1s region (Fig. S4†). Thus, the detailed formation process of VCQDs could be proposed as follows. The V_2C MXene could not remain stable and the C–V bonds were easily broken during the formation process of VCQDs, leading to the formation of C atoms with unsaturated bonds and oxidized V species.[38,42,43] These C atoms with unsaturated bonds in the carbon layer reacted with each other and formed a stable graphitic structure.[38] Meanwhile, lots of oxygenated groups such as C–OH and COOH were introduced under such oxidation conditions.[38] The oxidized V species underwent coordination with oxygenated groups on the graphitic structure, resulting in the formation of VO_x species on VCQDs.[44] XPS survey spectra demonstrated that only ~9% of vanadium atoms in V_2C MXene were retained on VCQDs because of the vanished C–V bonds and the limited content of oxygenated groups on VCQDs for oxidized V species binding and subsequent formation of VO_x species (Fig. S5†). These VCQDs with enriched oxygenated groups exhibited relatively high dispersibility in water (Fig. S6†). The stability of VCQDs against various physiological solutions including water and saline was explored *via* dialysis. Results of inductively coupled

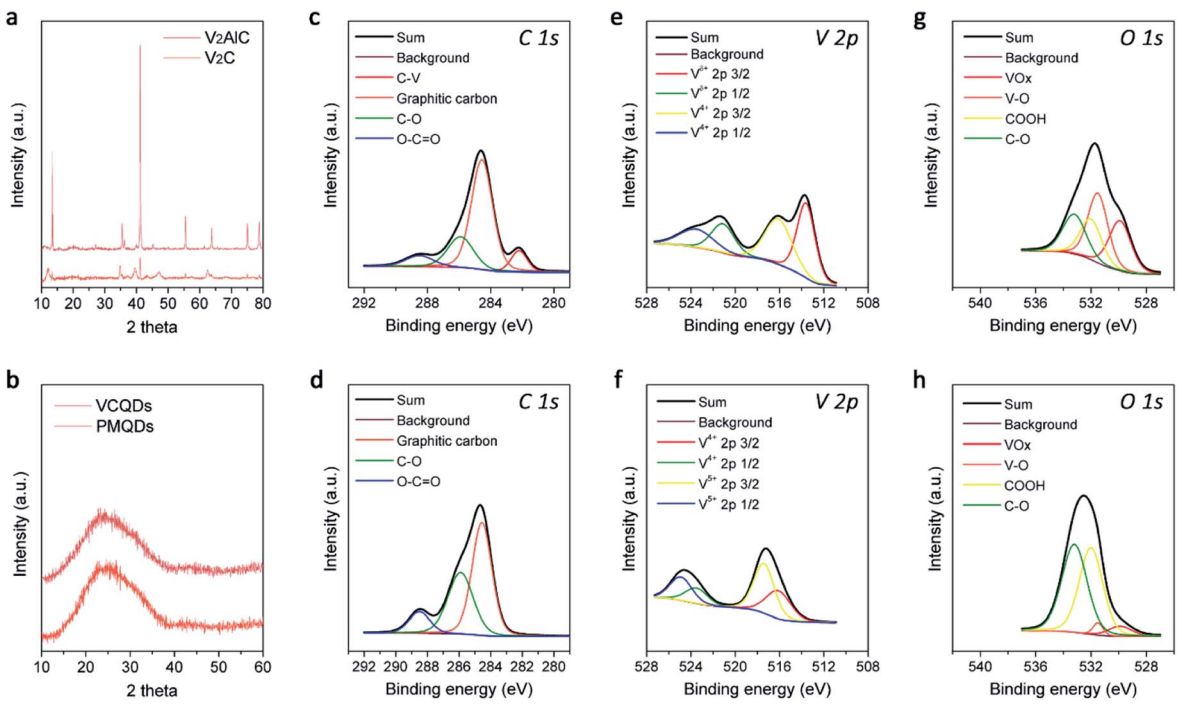

Fig. 2 Characterization of VCQDs. PXRD patterns of V_2AlC and V_2C MXene (a), as well as VCQDs and PMQDs (b). C 1s (c), V 2p (e), and O 1s (g) XPS spectra of V_2C MXene. C 1s (d), V 2p (f), and O 1s (h) XPS spectra of VCQDs.

plasma mass spectrometry (ICP-MS) revealed that a negligible amount of V was released from VCQDs even when the co-incubation period was prolonged to 7 days, indicating the high stability of these VCQDs in the above physiological solutions (data not shown). Moreover, the stability of VCQDs was further verified by XPS analysis (Fig. S7†).

In order to investigate the US-triggered ROS generating ability of VCQDs, electron spin resonance (ESR) was adopted to explore the generation of $^1O_2$ and $^{\bullet}OH$ by using TEMP and DMPO as the trapping agents, respectively. Fig. 3a and b illustrate the dose-dependent and time-dependent increase in ESR spectra obtained upon US irradiation of VCQDs with TEMP. The ESR signals displayed a typical spectrum characteristic of the TEMP/$^1O_2$ adducts, while a negligible ESR signal could be detected for samples containing the spin probe and VCQDs without US irradiation or the irradiated spin probe alone. These results indicated that the US-triggered generation of $^1O_2$ by VCQDs occurred in a concentration-dependent manner and an irradiation period-dependent manner. As for $^{\bullet}OH$ detection, similar results could be observed by using DMPO as the spin probe (Fig. 3c and d). These results demonstrated that VCQDs exhibited obvious US-triggered ROS generating capacity. Compared with the classical sonosensitizer, nano-TiO_2, the generation of $^1O_2$ and $^{\bullet}OH$ by VCQDs was much higher under the same US irradiation conditions. Quantitatively, the TEMP/$^1O_2$ and DMPO/$^{\bullet}OH$ signal intensities of VCQDs increased by 832.91% and 232.75% compared with those of nano-TiO_2, indicating that VCQDs could serve as high-efficacy sonosensitizers (Fig. 3k).

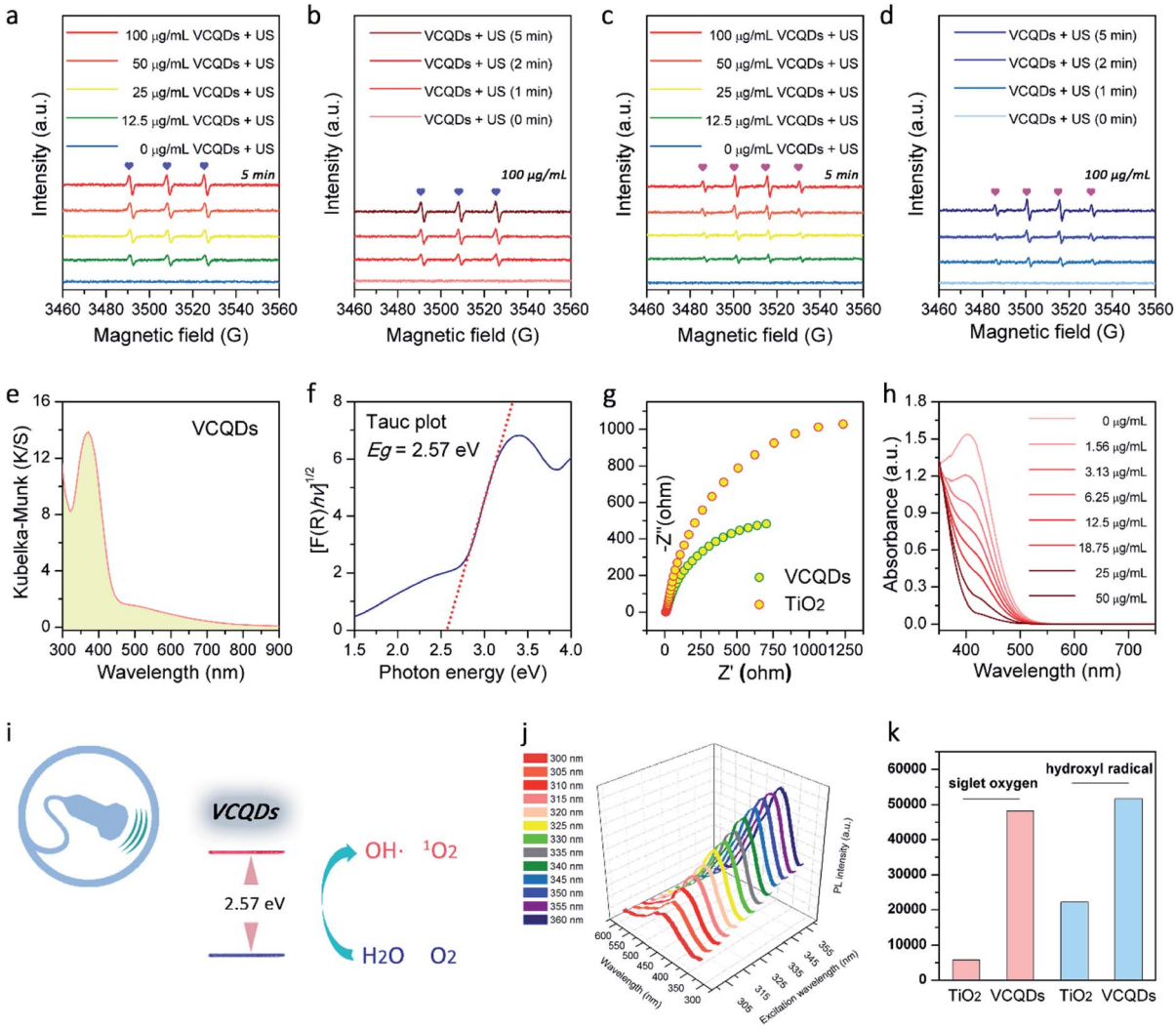

Fig. 3 Sonodynamic activity of VCQDs and related mechanisms. ESR spectra demonstrating concentration-dependent (a) and time-dependent (b) $^1O_2$ generation of VCQDs (100 μg mL^{-1}) under US irradiation (1.0 MHz, 0.5 W cm^{-2}, duty cycle: 50%, 5 min). ESR spectra demonstrating concentration-dependent (c) and time-dependent (d) $^{\bullet}OH$ generation of VCQDs (100 μg mL^{-1}) under US irradiation (1.0 MHz, 0.5 W cm^{-2}, duty cycle: 50%, 5 min). TEMP and DMPO are used as the trapping agents to investigate the generation of $^1O_2$ and $^{\bullet}OH$, respectively. The absorption spectrum transformed from the UV-vis diffuse reflectance spectrum by using the Kubelka–Munk function (e) and Tauc plot (f) of VCQDs. Nyquist plots of VCQDs and TiO_2 obtained from EIS measurements (g). Concentration-dependent GSH depletion abilities of VCQDs by using DTNB as the indicator of sulphydryl (–SH) in GSH (h). Schematic illustration of the sonodynamic mechanism of VCQDs under US irradiation (i). PL spectra of VCQDs under different excitations (j). The ROS generating abilities of VCQDs and TiO_2 quantified by the ESR signal intensities (k).

The UV-vis diffuse reflectance spectrum and corresponding absorption spectrum transformed by the Kubelka–Munk function were further recorded to better understand the sonodynamic performance of VCQDs (Fig. 3e and S8†). The bandgap energy of a sonosensitizer describes the energy needed to excite an electron from the valence band to the conduction band. Generally, a reduced bandgap can result in enhanced ROS generation during SDT. The Tauc plots presented in Fig. 3f and S9† were used to determine the band gap energies of VCQDs and commercial nano-TiO_2. The bandgap of VCQDs was determined to be 2.57 eV, much lower than that of commercial nano-TiO_2 (3.09 eV). During SDT, the US-triggered ROS generation is initiated by the sonoluminescence effect. The sonoluminescence is the emission of light in the ultraviolet and visible regions, which is produced by the cavitation-induced bubble collapse upon therapeutic US irradiation.[45–47] The sonoluminescence can activate the sonosensitizers *via* an energy transfer process for ROS generation. Hence, bandgap narrowing can allow sonosensitizers to be activated in a more visible band and facilitate the generation of electron–hole pairs for the subsequent activation of surrounding O_2 and H_2O molecules to produce ROS.[48,49] Additionally, the charge recombination dynamics of both VCQDs and TiO_2 have been investigated by time-resolved photoluminescence (TR-PL) spectroscopy. Compared with TiO_2, VCQDs showed a longer photoluminescence lifetime, indicating the mitigated charge recombination (Fig. S10†). Furthermore, the charge transfer capacity and carrier separation efficacy of VCQDs were investigated by electrochemical impedance spectroscopy (EIS). As shown in Fig. 3g, the Nyquist plots of VCQDs exhibited a smaller semicircle than that of commercial nano-TiO_2, indicating the more efficient migration/separation of electron–hole pairs of VCQDs. All these exciting results indicated the outstanding US-mediated ROS-generating ability of VCQDs. Moreover, the V^{5+} on VCQDs endowed them with efficient GSH depletion properties.[50] As shown in Fig. 3h and S11,† with increasing concentration of VCQDs, the GSH depletion was significantly enhanced. Similar to other CDs, these VCQDs exhibited photoluminescence (PL) properties with PL excitation (PLE) and PL peaks at 360 nm and 445 nm, respectively (Fig. 3j and S12†). Considering their further bio-related uses, VCQDs were further modified with poly(ethylene glycol) (PEG). The modification of nanomaterials with PEG can reduce the reticuloendothelial system (RES) uptake and increase the blood circulation time by diminishing their association with nontargeted serum and tissue proteins.[51] Moreover, the PEG functionalization of ultrasmall nanomaterials can efficiently increase their tumor accumulation caused by the enhanced permeability and retention (EPR) effect and prolonged body retention.[51] Therefore, VCQDs were further modified with PEG *via* the interaction between graphitic carbon and terminal phospholipid groups of mPEG-DSPE, which were termed PMQDs (Fig. S13†). Generally, a graphitic carbon-based nanostructure decorated with oxygenated groups contains a mixture of sp^2 and sp^3 hybridized carbon atoms, and the ultrasmall sp^2-hybridized domains are isolated within the sp^3 carbon matrix, and the local hydrophobic sp^2 hybridized domains can be utilized for phospholipid binding.[25,52] As shown in Fig. S14,† compared with that of VCQDs, the ζ potential value of PMQDs exhibited a significant increase, demonstrating successful PEGylation. Moreover, the PXRD pattern of PMQDs indicated that the graphitic carbon cores were well preserved after PEGylation (Fig. 2b). Significantly, the non-covalent PEGylation of VCQDs showed a negligible influence on the generation of $^1O_2$ and $^{\cdot}OH$ upon US irradiation (Fig. S15†).

The elevated Nrf2/ARE antioxidant mechanism in cancer cells neutralizes intracellular ROS and antagonizes the therapeutic efficacy of ROS-mediated anticancer therapies. Accordingly, the downstream antioxidant enzymes of Nrf2 were expressed at high levels in numerous human cancers, such as breast cancer, as compared with normal tissues.[53,54] Thus, triple-negative breast cancer cells (MDA-MB-231) were selected as a typical cell line for subsequent studies. Considering that NQO1 and HO-1 were two representative downstream antioxidant enzymes of Nrf2, we first used publicly available databases to analyze the clinical-related associations between NQO1/HO-1 and breast cancer (Fig. 4a–d). Analysis of data from the TNMplot database showed higher expression of NQO1 and HO-1 in breast cancer samples than that of normal controls.[55] Analysis of data from the Kaplan–Meier Plotter showed that the overall survival rate of breast cancer patients with high expression of NQO1 and HO-1 was significantly lower than that of breast cancer patients with low expression of NQO1 and HO-1.[56] These analyses indicated that the downstream antioxidant enzymes of Nrf2 including NQO1 and HO-1 did have close associations with pathological changes in breast cancer. Encouraged by above results, we first investigated the effects of PMQDs on the Nrf2 antioxidant program of MDA-MB-231 cells. The cellular uptake of PMQDs was first explored. Although PMQDs could emit blue fluorescence, the fluorescence was too weak for intracellular observation. Indeed, negligible fluorescence from PMQDs could be detected under the same parameters of the confocal microscope used for DAPI fluorescent probes (data not shown). Hence, PMQDs were functionalized with DSPE-PEG-Cy5 to result in fluorescent Cy5-PMQDs. The successful construction of Cy5-PMQDs was confirmed *via* PL spectra (Fig. S17†). As shown in Fig. 4e, Cy5-PMQDs could be effectively internalized by MDA-MB-231 cells in a time-dependent manner. Western blot analysis in Fig. 4i and k indicated that PMQDs could markedly suppress the expression of Nrf2 and its downstream antioxidant enzymes such as NQO1 and HO-1 in a concentration-dependent manner and an incubation period-dependent manner, which could be further verified by quantitative real-time PCR (qRT-PCR) analysis (Fig. 4l and m). Using immunofluorescence imaging, we found that an obvious decrease in the levels of cytoplasmic Nrf2 and its nuclear translocation could be observed upon PMQD treatment (Fig. 4f and g). Typically, the excess intracellular ROS liberates Nrf2 from its cytoplasmic repressor Keap1 and provokes the accumulation of Nrf2 in the nucleus for the activation of the expression of a set of detoxifying and antioxidant enzyme genes.[57] Under normal conditions, Nrf2 is constantly degraded *via* the ubiquitin-proteasome pathway in a Keap1-dependent manner.[58] It has been well demonstrated that V^{5+} exposure could upregulate the

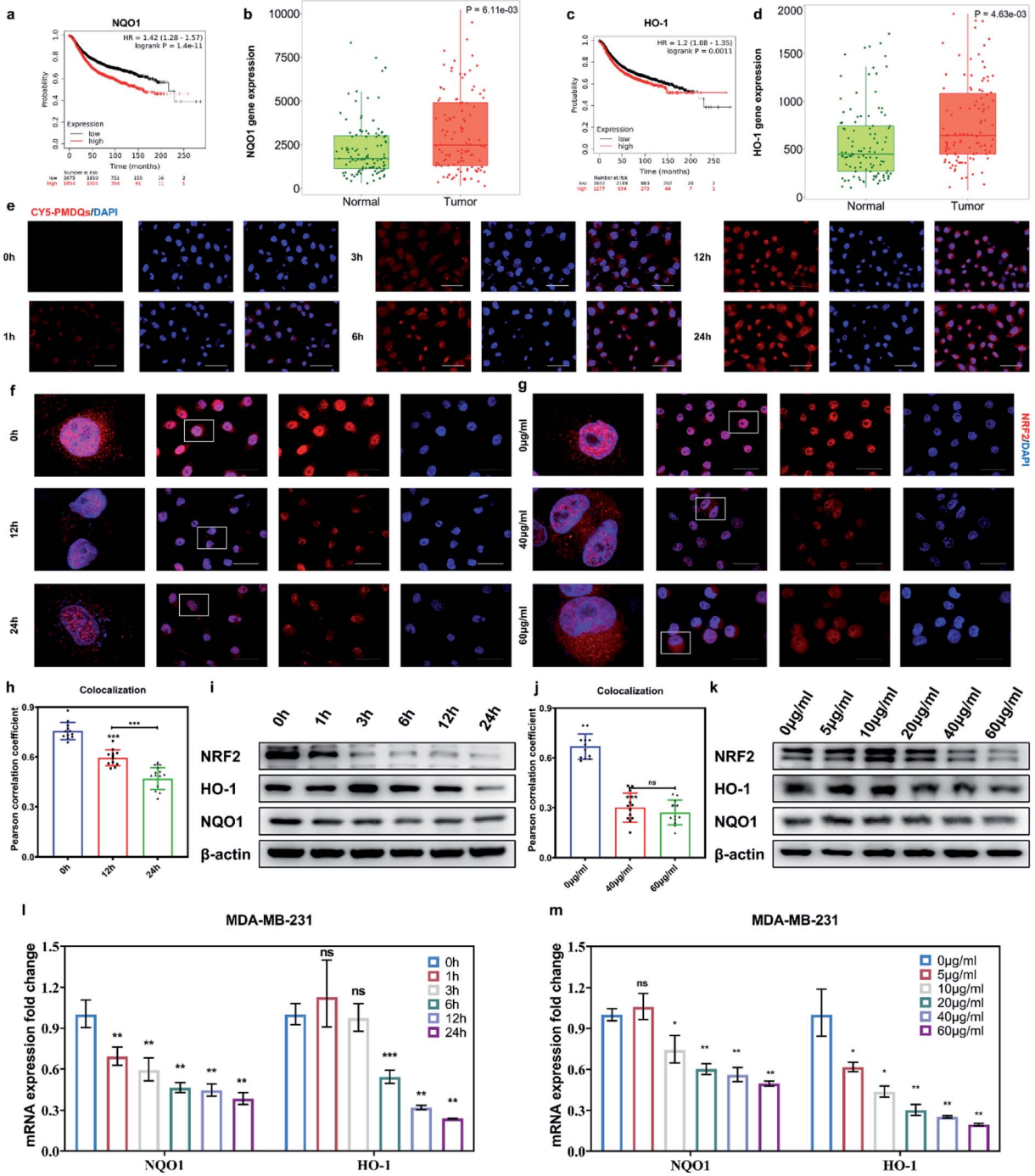

Fig. 4 PMQDs hindering the Nrf2/ARE antioxidant program *in vitro*. Kaplan–Meier plots of distant relapse-free survival of patients, with low (n = 3075) or high (n = 1854) NQO1 mRNA levels by the auto select best cutoff in Kaplan–Meier Plotter (a). Kaplan–Meier plots of distant relapse-free survival of patients, with low (n = 3652) or high (n = 1277) HO-1 mRNA levels by the auto select best cutoff in Kaplan–Meier Plotter (c). Data are obtained from the Kaplan–Meier plotter database. Differences between two survival curves are analyzed using the log-rank (Mantel–Cox) test. HR and P are adopted from the Kaplan–Meier Plotter. NQO1 (b) and HO-1 (d) are overexpressed in breast invasion carcinoma tissues than adjacent normal tissues in TNMplot database (RNA-seq, $P = 6.11 \times 10^{-3}$ for NQO1 and $P = 4.63 \times 10^{-3}$ for HO-1). $P < 0.05$ is recognized as statistically significant. Time-dependent cellular internalization imaging of Cy5-PMQDs (e). Scale bars are equal to 50 μm. Time-dependent (f) and concentration-dependent (g) confocal imaging of immunofluorescence staining of Nrf2 (red) in MDA-MB-231 cells treated with PMQDs. Scale bars are equal to 50 μm. Time-dependence (i) and concentration-dependence (k) of western blot analysis of MDA-MB-231 cells treated with PMQDs. (h) Pearson's co-localization coefficient between Nrf2 and DAPI in the depicted cells shown in (f). (j) Pearson's co-localization coefficient between Nrf2 and DAPI in the depicted cells shown in (g). Error bars represent standard deviation from the mean. A total of 12 individual cells (4 fields per experiment, 3 individual cells per field) are used for analysis. Time-dependence (l) and concentration-dependence (m) of qRT-PCR analysis of MDA-MB-231 cells treated with PMQDs. The qRT-PCR results are expressed as the mean ± error (n = 3). Asterisks indicate statistically significant differences (*P < 0.05, **P < 0.01, and ***P < 0.001).

intracellular Keap1 and promote Nrf2 degradation, leading to the reduction of antioxidant capacity.[35,36] Since PMQDs were enriched with V^{5+} species, they could perturb the Nrf2/ARE antioxidant mechanism and downregulate the expression of the downstream antioxidant enzymes of Nrf2 such as NQO1 and HO-1. Additionally, we assessed whether PMQDs could alter the intracellular GSH levels. As shown in Fig. 5e and f and S18,† with increasing concentration of PMQDs, the GSH levels inside cells decreased significantly, indicating that PMQDs could effectively deplete intracellular GSH.

The SDT efficacy of PMQDs was then investigated *in vitro*. MTT assays associated with MDA-MB-231 cells without US irradiation revealed that cellular viabilities were moderately hindered by PMQDs at high concentrations (Fig. 5a). Results of flow cytometry indicated that excess intracellular ROS were generated when cells were treated with PMQDs (Fig. 5g and S19†). The increased intracellular ROS levels could be attributed to the PMQD-induced reduction of the increased antioxidant capacity of cancer cells. Upon US irradiation (1 MHz, 1 W cm^{-2}, duty cycle: 50%, 1 min), PMQD-mediated SDT induced significantly enhanced cytotoxicity. Results of flow cytometry further demonstrated that PMQDs could significantly increase the intracellular ROS levels upon US irradiation, indicating that PMQDs had an excellent US-induced ROS-generating ability *in vitro*. The ROS-generating ability of PMQDs could also be visualized by fluorescence microscopy (Fig. 5h). Furthermore, cell-killing effects of PMQDs with or without US irradiation were verified by Annexin V-FITC apoptosis detection (Fig. 5b and S20†). The anti-proliferative effects of PMQDs were then investigated by a cell colony formation assay. As shown in Fig. 5d,

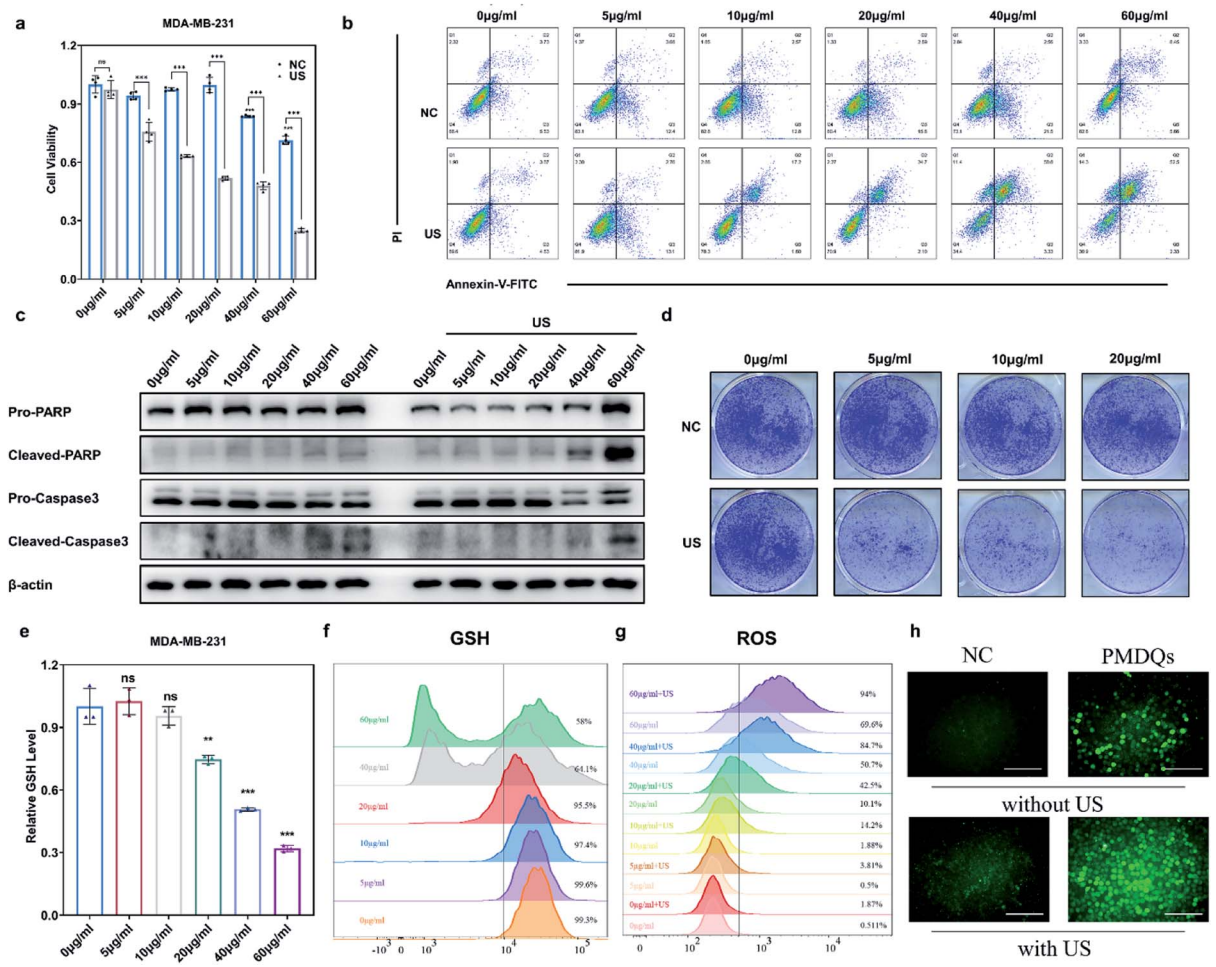

Fig. 5 *In vitro* SDT efficacy of PMQDs. Cytotoxicity and SDT efficacy (1.0 MHz, 1 W cm^{-2}, duty cycle: 50%) of PMQDs (a). Error bars represent standard deviation from the mean ($n = 4$). Asterisks indicate statistically significant differences (*$P < 0.05$, **$P < 0.01$, ***$P < 0.001$). Apoptosis/necrosis analysis of SDT efficacy based on flow cytometry in MDA-MB-231 cells incubated with PMQDs upon US (1.0 MHz, 1 W cm^{-2}, duty cycle: 50%) irradiation (b). The expression of cleaved PARP, cleaved caspase-3, and β-actin in MDA-MB-231 cells incubated with PMQDs examined by western blot analysis (c). Representative digital photographs of the colony formation assay of MDA-MB-231 cells treated with PMQDs under US (1.0 MHz, 1 W cm^{-2}, duty cycle: 50%) irradiation (d). Quantitative analysis of GSH levels in MDA-MB-231 cells incubated with PMQDs (e). Flow cytometry analysis of GSH levels in MDA-MB-231 cells incubated with PMQDs (f). Flow cytometry analysis of US-induced ROS generation in MDA-MB-231 cells incubated with PMQDs upon US (1.0 MHz, 1 W cm^{-2}, duty cycle: 50%) irradiation (g). Fluorescence images of DCFH-DA stained MDA-MB-231 cells treated with PMQDs under US (1.0 MHz, 1 W cm^{-2}, duty cycle: 50%) irradiation (h). Scale bars are equal to 200 μm. Error bars represent standard deviation from the mean ($n = 3$). Asterisks indicate statistically significant differences (*$P < 0.05$, **$P < 0.01$, ***$P < 0.001$).

MDA-MB-231 cells co-treated with PMQDs and US irradiation displayed far fewer colonies even at a low concentration of 20 μg mL^{-1}, indicating the high US-triggered anti-proliferative ability of PMQDs. Western blot analysis of the expression of apoptosis biomarkers (Caspase 3 and PARP) further revealed that MDA-MB-231 cells were killed by PMQDs *via* an apoptosis process (Fig. 5c). All these results demonstrated that PMQDs could efficiently generate ROS upon US irradiation to kill cancer cells and hinder the tumor Nrf2 antioxidant program *in vitro*.

We then explored the biodistribution of these PMQDs in MDA-MB-231 tumor-bearing mice. Time-dependent *in vivo* fluorescence imaging was carried out to monitor the biodistribution of Cy5-PMQDs visually. As shown in Fig. 6b, Cy5-PMQDs could be easily detected in tumors within 6 h after intravenous (i.v.) injection. Significantly, the fluorescence signal from Cy5-PMQDs could also be detected in the tumors even at 72 h post-injection, suggesting their long blood circulation time and satisfactory tumor accumulation (Fig. 6c). The above results were further verified by ICP-MS *ex vivo* (Fig. 6d). Moreover, most of the PMQDs remained in the kidneys during the experimental period, and the fluorescent signals from Cy5-MOF QDs as well as the levels of V in other organs decreased over time. The above biodistribution analysis indicated that the main clearance pathway of PMQDs was a renal one, which could minimize the potential long-term toxicity. We further investigated the *in vivo* anticancer efficacy of PMQDs. Balb/c nude mice bearing MDA-MB-231 tumors were randomly divided into four groups and defined as the control, US alone, PMQDs alone, and PMQDs +

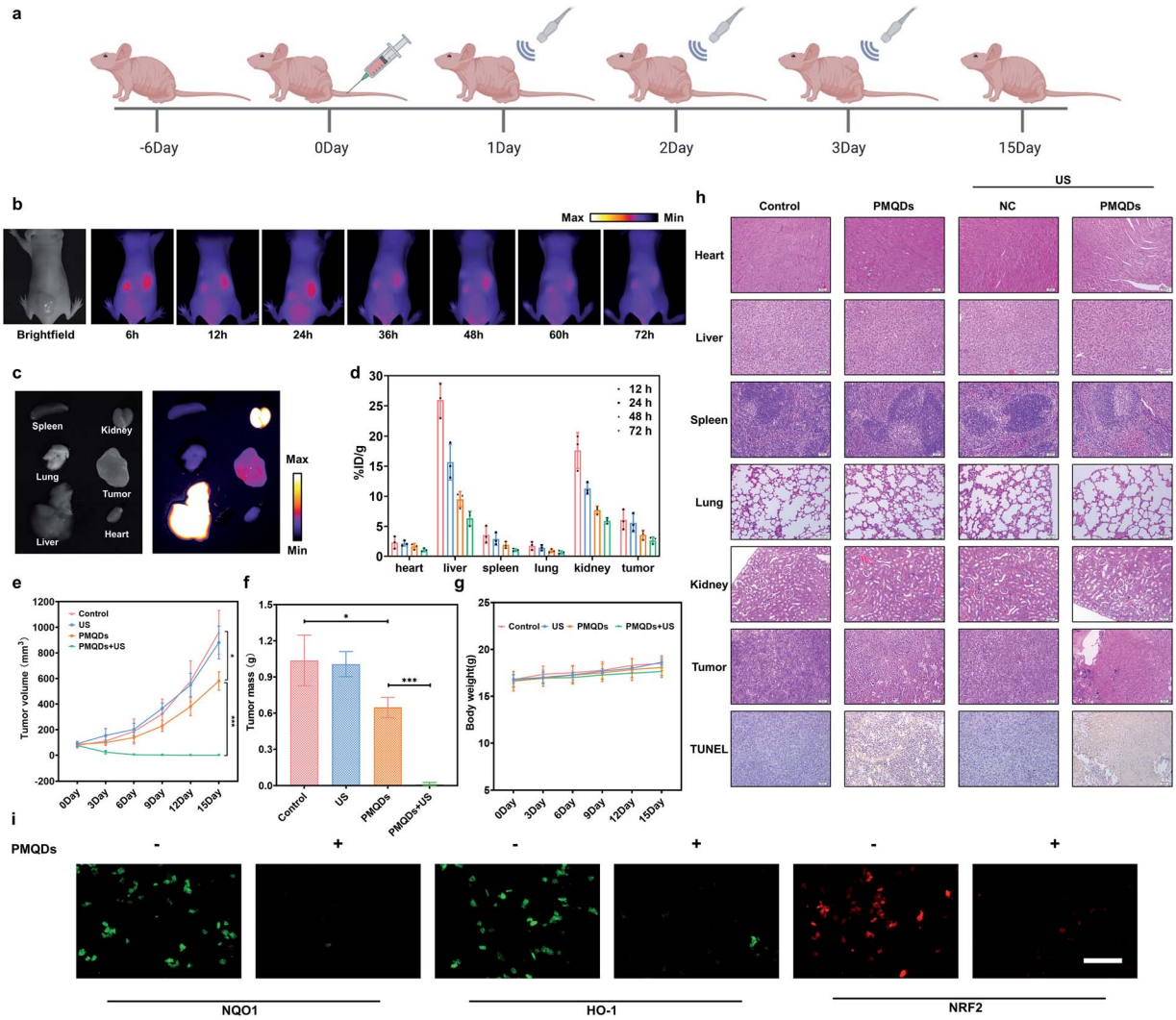

Fig. 6 *In vivo* SDT efficacy of PMQDs. Schematic illustration of the PMQD-mediated SDT process (a). Created with BioRender.com. Time-dependent *in vivo* (b) and *ex vivo* (c) fluorescence imaging of tumor-bearing mice after i.v. injection of Cy5-PMQDs. Biodistribution analysis of PMQDs from tumor-bearing mice after i.v. injection *via* ICP-MS (d). Tumor growth curves of the tumor-bearing mice after various treatments (e). Tumor masses collected from the tumor-bearing mice at 15 days post initiation of various treatments (f). Bodyweight changes of the mice after various treatments (g). H&E/TUNEL-stained images of tumor slices collected from various groups after various treatments and H&E staining images of major organs of the mice after various treatments (h). Scale bars are equal to 50 μm. NQO1, HO-1, and Nrf2-stained immunofluorescence images of tumor slices collected from various groups after various treatments (i). Scale bars are equal to 200 μm. Error bars represent standard deviation from the mean ($n = 3$). Asterisks indicate statistically significant differences (*$P < 0.05$, **$P < 0.01$, ***$P < 0.001$).

US, respectively. At 12 h after i.v. injection of PMQDs, the tumors were treated with US irradiation (1 MHz, 2 W cm^{-2}, duty cycle: 50%, 3 min) and repeated daily for 3 days (Fig. 6a). Tumor volumes and weights were measured to explore the anticancer efficacy of PMQDs *in vivo* (Fig. 6e and f). The tumors of mice in the PMQD group were smaller than those in the control group, indicating that PMQDs showed a moderate therapeutic effect. The therapeutic effect of PMQDs could be attributed to the damaged antioxidant defense system of cancer cells as indicated by immunofluorescence images of tumor slices (Fig. 6i). Upon US irradiation, PMQD-mediated SDT induced significantly enhanced suppressive effects on tumor growth. Notably, complete tumor elimination occurred in the group of PMQDs + US, and no tumor relapse was observed in further days. In order to better understand the therapeutic efficacy upon various treatments, H&E staining and TUNEL staining were further performed. As expected, the group of PMQDs showed a moderate level of cancer cell apoptosis, whereas the group of PMQDs + US showed the highest level of cancer cell apoptosis among all experimental groups (Fig. 6h and S21†). Additionally, mice in all groups showed negligible differences in body weight during the whole experimental period (Fig. 6g). H&E staining images of major exposed organs from mice after various treatments indicated the high biocompatibility of PMQDs (Fig. 6h).

Given the excellent therapeutic efficacy, we then investigated the biosafety of these PMQDs in detail. As shown in Fig. S22a,† HaCaT cells (human epithelial cells) were used to investigate the cytotoxicity of PMQDs towards normal cells. The results indicated that PMQDs showed negligible cytotoxicity towards normal cells even at doses higher than those required for SDT. Recently, Chen and co-workers have found the antioxidative behaviors of V_2C MXene.[34] These vanadium-based nanomaterials possessed high biocompatibility and exhibited robust *in vitro* cytoprotection against oxidative stress. The vanadium species in the V_2C MXenes were mainly V^{2+}, V^{3+}, and V^{4+}, which played major roles in the antioxidant activity. However, in the present study, only the high valence V species including V^{4+} and V^{5+} were present on VCQDs. These V^{5+} species on VCQDs could not only endow them with efficient GSH depletion properties through GSH-mediated reduction, but also perturb the Nrf2/ARE antioxidant mechanism in cells. More importantly, the elevated Nrf2/ARE antioxidant mechanism in cancer cells makes them highly sensitive to Nrf2/ARE antioxidant program disturbance.[14] Therefore, PMQDs showed selective cytotoxicity towards cancer cells. Afterwards, the *in vivo* toxicity of PMQDs was further investigated in healthy mice by body weight measurement, histological analysis, and blood routine test at the dose required for SDT (10 mg kg^{-1}) and higher doses (25 mg kg^{-1} and 50 mg kg^{-1}). As shown in Fig. S22b,† mice in the test group exhibited negligible differences in body weight, eating, drinking, and activity. Moreover, H&E staining images of major organs from mice in the test group suggested the high biocompatibility of PMQDs (Fig. S22e†). Additionally, results of a routine blood test indicated that there were no significant differences between the test group and the control group (Fig. S22d†). All these results demonstrated the high biocompatibility of PMQDs.

Conclusions

In summary, PMQDs could not only efficiently generate ROS upon US irradiation, but also perturb the tumor antioxidant mechanism for enhanced SDT of cancer. With efficient migration/separation of electron–hole pairs and narrow bandgap, these PMQDs showed high US-triggered ROS generating efficacy. Besides, PMQDs could hinder the Nrf2/ARE antioxidant program, and decrease the expression of related downstream antioxidant enzymes such as NQO1 and HO-1, and thus amplify the cytotoxicity of ROS during SDT. The efficient Nrf2 antioxidant program hindrance of cancer cells and high ROS generating efficacy of PMQDs highlight their promise as high-efficacy SDT nanoagents.

Data availability

All experimental and characterization data are available in the ESI.†

Author contributions

H. W., X. L., and J. R. conceived and designed the study. H. W., X. Y., and J. F. performed the synthesis and characterization of the materials. X. L. performed the cell culture studies. X. L., H. W., and J. F. performed the animal studies. H. W., X. L., D. L., J. R., and X. Q. analysed the experimental data and wrote the paper. All the authors discussed the results and commented on the manuscript. J. R. and X. Q. supervised the whole project.

Conflicts of interest

There are no conflicts to declare.

Acknowledgements

This work was supported by the National Key R&D Program of China (2021YFF1200701 and 2019YFA0709202), the National Natural Science Foundation of China (91856205, 21871249, 21820102009, and 22105197), and the Key Program of Frontier of Sciences (CAS QYZDJ-SSW-SLH052). Schematics in Fig. 1a and c, 6a, and S1† were created with BioRender.com (**https://biorender.com/**) and used with permission. The graphic for the Table of Contents was created by Figdraw (**https://www.figdraw.com/**) as well as BioRender.com (**https://biorender.com/**) and used with permission.

Notes and references

1 X. Qian, Y. Zheng and Y. Chen, Micro/nanoparticle-augmented sonodynamic therapy (SDT): Breaking the depth shallow of photoactivation, *Adv. Mater.*, 2016, **28**, 8097–8129.

2 F. Gong, L. Cheng, N. Yang, Y. Gong, Y. Ni, S. Bai, X. Wang, M. Chen, Q. Chen and Z. Liu, Preparation of $TiH_{1.924}$ nanodots by liquid-phase exfoliation for enhanced sonodynamic cancer therapy, *Nat. Commun.*, 2020, **11**, 3712.

3 X. Wang, X. Zhong, L. Bai, J. Xu, F. Gong, Z. Dong, Z. Yang, Z. Zeng, Z. Liu and L. Cheng, Ultrafine titanium monoxide (TiO_{1+x}) nanorods for enhanced sonodynamic therapy, *J. Am. Chem. Soc.*, 2020, **142**, 6527–6537.

4 V. G. Deepagan, D. G. You, W. Um, H. Ko, S. Kwon, K. Y. Choi, G.-R. Yi, J. Y. Lee, D. S. Lee, K. Kim, I. C. Kwon and J. H. Park, Long-circulating Au-TiO_2 nanocomposite as a sonosensitizer for ROS-mediated eradication of cancer, *Nano Lett.*, 2016, **16**, 6257–6264.

5 H. Chen, X. Zhou, Y. Gao, B. Zheng, F. Tang and J. Huang, Recent progress in development of new sonosensitizers for sonodynamic cancer therapy, *Drug Discovery Today*, 2014, **19**, 502–509.

6 X. Pan, L. Bai, H. Wang, Q. Wu, H. Wang, S. Liu, B. Xu, X. Shi and H. Liu, Metal–organic-framework-derived carbon nanostructure augmented sonodynamic cancer therapy, *Adv. Mater.*, 2018, **30**, 1800180.

7 S. Liang, X. Deng, Y. Chang, C. Sun, S. Shao, Z. Xie, X. Xiao, P. a. Ma, H. Zhang, Z. Cheng and J. Lin, Intelligent hollow Pt-CuS janus architecture for synergistic catalysis-enhanced Sonodynamic and Photothermal Cancer Therapy, *Nano Lett.*, 2019, **19**, 4134–4145.

8 A. Ma, H. Chen, Y. Cui, Z. Luo, R. Liang, Z. Wu, Z. Chen, T. Yin, J. Ni, M. Zheng and L. Cai, Metalloporphyrin complex-based nanosonosensitizers for deep-tissue tumor theranostics by noninvasive sonodynamic therapy, *Small*, 2019, **15**, 1804028.

9 X. Qian, X. Han and Y. Chen, Insights into the unique functionality of inorganic micro/nanoparticles for versatile ultrasound theranostics, *Biomaterials*, 2017, **142**, 13–30.

10 F. Gong, L. Cheng, N. Yang, O. Betzer, L. Feng, Q. Zhou, Y. Li, R. Chen, R. Popovtzer and Z. Liu, Ultrasmall oxygen-deficient bimetallic oxide $MnWO_x$ nanoparticles for depletion of endogenous GSH and enhanced sonodynamic cancer therapy, *Adv. Mater.*, 2019, **31**, 1900730.

11 C. Gorrini, I. S. Harris and T. W. Mak, Modulation of oxidative stress as an anticancer strategy, *Nat. Rev. Drug Discovery*, 2013, **12**, 931–947.

12 J. Wang, Q. Lu, J. Cai, Y. Wang, X. Lai, Y. Qiu, Y. Huang, Q. Ke, Y. Zhang, Y. Guan, H. Wu, Y. Wang, X. Liu, Y. Shi, K. Zhang, M. Wang and A. P. Xiang, Nestin regulates cellular redox homeostasis in lung cancer through the Keap1–Nrf2 feedback loop, *Nat. Commun.*, 2019, **10**, 5043.

13 T. Nguyen, P. Nioi and C. B. Pickett, The Nrf2-antioxidant response element signaling pathway and its activation by oxidative stress, *J. Biol. Chem.*, 2009, **284**, 13291–13295.

14 G. M. DeNicola, F. A. Karreth, T. J. Humpton, A. Gopinathan, C. Wei, K. Frese, D. Mangal, K. H. Yu, C. J. Yeo, E. S. Calhoun, F. Scrimieri, J. M. Winter, R. H. Hruban, C. Iacobuzio-Donahue, S. E. Kern, I. A. Blair and D. A. Tuveson, Oncogene-induced Nrf2 transcription promotes ROS detoxification and tumorigenesis, *Nature*, 2011, **475**, 106–109.

15 X. Sun, Z. Ou, R. Chen, X. Niu, D. Chen, R. Kang and D. Tang, Activation of the p62-Keap1-NRF2 pathway protects against ferroptosis in hepatocellular carcinoma cells, *Hepatology*, 2016, **63**, 173–184.

16 M. Dodson, R. Castro-Portuguez and D. D. Zhang, NRF2 plays a critical role in mitigating lipid peroxidation and ferroptosis, *Redox Biol.*, 2019, **23**, 101107.

17 M. B. Sporn and K. T. Liby, NRF2 and cancer: the good, the bad and the importance of context, *Nat. Rev. Cancer*, 2012, **12**, 564–571.

18 E. Kansanen, S. M. Kuosmanen, H. Leinonen and A.-L. Levonen, The Keap1-Nrf2 pathway: Mechanisms of activation and dysregulation in cancer, *Redox Biol.*, 2013, **1**, 45–49.

19 G. Hong, S. Diao, A. L. Antaris and H. Dai, Carbon nanomaterials for biological imaging and nanomedicinal therapy, *Chem. Rev.*, 2015, **115**, 10816–10906.

20 V. Georgakilas, J. A. Perman, J. Tucek and R. Zboril, Broad family of carbon nanoallotropes: Classification, chemistry, and applications of fullerenes, carbon dots, nanotubes, graphene, nanodiamonds, and combined superstructures, *Chem. Rev.*, 2015, **115**, 4744–4822.

21 N. Panwar, A. M. Soehartono, K. K. Chan, S. Zeng, G. Xu, J. Qu, P. Coquet, K.-T. Yong and X. Chen, Nanocarbons for biology and medicine: Sensing, imaging, and drug delivery, *Chem. Rev.*, 2019, **119**, 9559–9656.

22 S. Zhu, Q. Meng, L. Wang, J. Zhang, Y. Song, H. Jin, K. Zhang, H. Sun, H. Wang and B. Yang, Highly photoluminescent carbon dots for multicolor patterning, sensors, and bioimaging, *Angew. Chem., Int. Ed.*, 2013, **52**, 3953–3957.

23 C. Xia, S. Zhu, T. Feng, M. Yang and B. Yang, Evolution and synthesis of carbon dots: From carbon dots to carbonized polymer dots, *Adv. Sci.*, 2019, **6**, 1901316.

24 S. Lu, L. Sui, J. Liu, S. Zhu, A. Chen, M. Jin and B. Yang, Near-infrared photoluminescent polymer–carbon nanodots with two-photon fluorescence, *Adv. Mater.*, 2017, **29**, 1603443.

25 H. Wang, D. Yu, J. Fang, Y. Zhou, D. Li, Z. Liu, J. Ren and X. Qu, Phenol-like group functionalized graphene quantum dots structurally mimicking natural antioxidants for highly efficient acute kidney injury treatment, *Chem. Sci.*, 2020, **11**, 12721–12730.

26 L. Li and T. Dong, Photoluminescence tuning in carbon dots: surface passivation or/and functionalization, heteroatom doping, *J. Mater. Chem. C*, 2018, **6**, 7944–7970.

27 G. Nocito, G. Calabrese, S. Forte, S. Petralia, C. Puglisi, M. Campolo, E. Esposito and S. Conoci, Carbon dots as promising tools for cancer diagnosis and therapy, *Cancers*, 2021, **13**, 1991.

28 H. Li, X. He, Z. Kang, H. Huang, Y. Liu, J. Liu, S. Lian, C. H. A. Tsang, X. Yang and S.-T. Lee, Water-soluble fluorescent carbon quantum dots and photocatalyst design, *Angew. Chem., Int. Ed.*, 2010, **49**, 4430–4434.

29 J. Ge, M. Lan, B. Zhou, W. Liu, L. Guo, H. Wang, Q. Jia, G. Niu, X. Huang, H. Zhou, X. Meng, P. Wang, C.-S. Lee, W. Zhang and X. Han, A graphene quantum dot photodynamic therapy agent with high singlet oxygen generation, *Nat. Commun.*, 2014, **5**, 4596.

30 S. Yang, X. Wang, P. He, A. Xu, G. Wang, J. Duan, Y. Shi and G. Ding, Graphene quantum dots with pyrrole N and pyridine N: Superior reactive oxygen species generation

efficiency for metal-free sonodynamic tumor therapy, *Small*, 2021, **17**, 2004867.

31 Z. Fu, N. Wang, D. Legut, C. Si, Q. Zhang, S. Du, T. C. Germann, J. S. Francisco and R. Zhang, Rational design of flexible two-dimensional MXenes with multiple functionalities, *Chem. Rev.*, 2019, **119**, 11980–12031.

32 M. Naguib, V. N. Mochalin, M. W. Barsoum and Y. Gogotsi, 25th anniversary article: MXenes: A new family of two-dimensional materials, *Adv. Mater.*, 2014, **26**, 992–1005.

33 X. Li, C. Wang, Y. Cao and G. Wang, Functional MXene materials: Progress of their applications, *Chem.–Asian J.*, 2018, **13**, 2742–2757.

34 W. Feng, X. Han, H. Hu, M. Chang, L. Ding, H. Xiang, Y. Chen and Y. Li, 2D vanadium carbide MXenzyme to alleviate ROS-mediated inflammatory and neurodegenerative diseases, *Nat. Commun.*, 2021, **12**, 2203.

35 Y. Ma, Y. Shi, Q. Wu and W. Ma, Epigallocatechin-3-gallate alleviates vanadium-induced reduction of antioxidant capacity via Keap1-Nrf2-sMaf pathway in the liver, kidney, and ovary of laying hens, *Biol. Trace Elem. Res.*, 2021, **199**, 2707–2716.

36 J. Wang, X. Huang, K. Zhang, X. Mao, X. Ding, Q. Zeng, S. Bai, Y. Xuan and H. Peng, Vanadate oxidative and apoptotic effects are mediated by the MAPK-Nrf2 pathway in layer oviduct magnum epithelial cells, *Metallomics*, 2017, **9**, 1562–1575.

37 S.-M. Bak, R. Qiao, W. Yang, S. Lee, X. Yu, B. Anasori, H. Lee, Y. Gogotsi and X.-Q. Yang, Na-ion intercalation and charge storage mechanism in 2D vanadium carbide, *Adv. Energy Mater.*, 2017, **7**, 1700959.

38 B. Wang, M. Wang, F. Liu, Q. Zhang, S. Yao, X. Liu and F. Huang, Ti_3C_2: An ideal co-catalyst?, *Angew. Chem., Int. Ed.*, 2020, **59**, 1914–1918.

39 S. Ji, B. Jiang, H. Hao, Y. Chen, J. Dong, Y. Mao, Z. Zhang, R. Gao, W. Chen, R. Zhang, Q. Liang, H. Li, S. Liu, Y. Wang, Q. Zhang, L. Gu, D. Duan, M. Liang, D. Wang, X. Yan and Y. Li, Matching the kinetics of natural enzymes with a single-atom iron nanozyme, *Nat. Catal.*, 2021, **4**, 407–417.

40 J.-G. Choi, The surface properties of vanadium compounds by X-ray photoelectron spectroscopy, *Appl. Surf. Sci.*, 1999, **148**, 64–72.

41 M. Naguib, J. Halim, J. Lu, K. M. Cook, L. Hultman, Y. Gogotsi and M. W. Barsoum, New two-dimensional niobium and vanadium carbides as promising materials for Li-ion batteries, *J. Am. Chem. Soc.*, 2013, **135**, 15966–15969.

42 Y. Liu, Y. Jiang, Z. Hu, J. Peng, W. Lai, D. Wu, S. Zuo, J. Zhang, B. Chen, Z. Dai, Y. Yang, Y. Huang, W. Zhang, W. Zhao, W. Zhang, L. Wang and S. Chou, In-situ electrochemically activated surface vanadium valence in V_2C MXene to achieve high capacity and superior rate performance for Zn-ion batteries, *Adv. Funct. Mater.*, 2021, **31**, 2008033.

43 W. Zhang, J. Peng, W. Hua, Y. Liu, J. Wang, Y. Liang, W. Lai, Y. Jiang, Y. Huang, W. Zhang, H. Yang, Y. Yang, L. Li, Z. Liu, L. Wang and S.-L. Chou, Architecting amorphous vanadium oxide/MXene nanohybrid via tunable anodic oxidation for high-performance sodium-ion batteries, *Adv. Energy Mater.*, 2021, **11**, 2100757.

44 M. Sathiya, A. S. Prakash, K. Ramesha, J. M. Tarascon and A. K. Shukla, V_2O_5-anchored carbon nanotubes for enhanced electrochemical energy storage, *J. Am. Chem. Soc.*, 2011, **133**, 16291–16299.

45 T. J. Matula, R. A. Roy, P. D. Mourad, W. B. McNamara III and K. S. Suslick, Comparison of multibubble and single-bubble sonoluminescence spectra, *Phys. Rev. Lett.*, 1995, **75**, 2602–2605.

46 V. Choi, M. A. Rajora and G. Zheng, Activating drugs with sound: mechanisms behind sonodynamic therapy and the role of nanomedicine, *Bioconjugate Chem.*, 2020, **31**, 967–989.

47 V. Vighetto, A. Troia, M. Laurenti, M. Carofiglio, N. Marcucci, G. Canavese and V. Cauda, Insight into sonoluminescence augmented by ZnO-functionalized nanoparticles, *ACS Omega*, 2022, **7**, 6591–6600.

48 S. Liang, B. Liu, X. Xiao, M. Yuan, L. Yang, P. a. Ma, Z. Cheng and J. Lin, A robust narrow bandgap vanadium tetrasulfide sonosensitizer optimized by charge separation engineering for enhanced sonodynamic cancer therapy, *Adv. Mater.*, 2021, **33**, 2101467.

49 S. Liang, X. Xiao, L. Bai, B. Liu, M. Yuan, P. a. Ma, M. Pang, Z. Cheng and J. Lin, Conferring Ti-based MOFs with defects for enhanced sonodynamic cancer therapy, *Adv. Mater.*, 2021, **33**, 2100333.

50 E. Sabbioni, G. Pozzi, S. Devos, A. Pintar, L. Casella and M. Fischbach, The intensity of vanadium(V)-induced cytotoxicity and morphological transformation in BALB/3T3 cells is dependent on glutathione-mediated bioreduction to vanadium(IV), *Carcinogenesis*, 1993, **14**, 2565–2568.

51 J. V. Jokerst, T. Lobovkina, R. N. Zare and S. S. Gambhir, Nanoparticle PEGylation for imaging and therapy, *Nanomedicine*, 2011, **6**, 715–728.

52 K. P. Loh, Q. Bao, G. Eda and M. Chhowalla, Graphene oxide as a chemically tunable platform for optical applications, *Nat. Chem.*, 2010, **2**, 1015–1024.

53 Y. Yang, Y. Zhang, Q. Wu, X. Cui, Z. Lin, S. Liu and L. Chen, Clinical implications of high NQO1 expression in breast cancers, *J. Exp. Clin. Cancer Res.*, 2014, **33**, 14.

54 E. C. Lien, C. A. Lyssiotis, A. Juvekar, H. Hu, J. M. Asara, L. C. Cantley and A. Toker, Glutathione biosynthesis is a metabolic vulnerability in PI(3)K/Akt-driven breast cancer, *Nat. Cell Biol.*, 2016, **18**, 572–578.

55 Á. Bartha and B. Győrffy, TNMplot.com: A Web Tool for the Comparison of Gene Expression in Normal, Tumor and Metastatic Tissues, *Int. J. Mol. Sci.*, 2021, **22**, 2622.

56 B. Győrffy, Survival analysis across the entire transcriptome identifies biomarkers with the highest prognostic power in breast cancer, *Comput. Struct. Biotechnol. J.*, 2021, **19**, 4101–4109.

57 D. D. Zhang, Mechanistic studies of the Nrf2-Keap1 signaling pathway, *Drug Metab. Rev.*, 2006, **38**, 769–789.

58 K. Taguchi, H. Motohashi and M. Yamamoto, Molecular mechanisms of the Keap1–Nrf2 pathway in stress response and cancer evolution, *Genes Cells*, 2011, **16**, 123–140.